Wave-Follower Field Measurements of the Wind-Input Spectral Function. Part II: Parameterization of the Wind Input

MARK A. DONELAN

Rosenstiel School of Marine and Atmospheric Science, University of Miami, Miami, Florida

ALEXANDER V. BABANIN

Faculty of Engineering and Industrial Sciences, Swinburne University of Technology, Melbourne, Australia

IAN R. YOUNG

Swinburne University of Technology, Melbourne, Australia

MICHAEL L. BANNER

School of Mathematics, University of New South Wales, Sydney, Australia

(Manuscript received 1 November 2005, in final form 17 January 2006)

ABSTRACT

Nearly all of the momentum transferred from wind to waves comes about through wave-induced pressure acting on the slopes of waves: known as form drag. Direct field measurements of the wave-induced pressure in airflow over water waves are difficult and consequently rare. Those that have been reported are for deep water conditions and conditions in which the level of forcing, measured by the ratio of wind speed to the speed of the dominant (spectral peak) waves, is quite weak, $U_{10}/c_p < 3$. The data reported here were obtained over a large shallow lake during the Australian Shallow Water Experiment (AUSWEX). The propagation speeds of the dominant waves were limited by depth and the waves were correspondingly steep. This wider range of forcing and concomitant wave steepness revealed some new aspects of the rate of wave amplification by wind, the so-called wind input source function, in the energy balance equation for wind-driven water waves. It was found that the exponential growth rate parameter (fractional energy increase per radian) depended on the slope of the waves, ak, vanishing as $ak \to 0$. For very strong forcing a condition of "full separation" occurs, where the airflow detaches from the crests and reattaches on the windward face leaving a separation zone over the leeward face and the troughs. In a sense, the outer flow does not "see" the troughs and the resulting wave-induced pressure perturbation is much reduced, leading to a reduction in the wind input source function relative to that obtained by extrapolation from more benign conditions. The source function parameterized on wave steepness and degree of separation is shown to be in agreement with previous field and laboratory data obtained in conditions of much weaker forcing and wave steepness. The strongly forced steady-state conditions of AUSWEX have enabled the authors to define a generalized wind input source function that is suitable for a wide range of conditions.

1. Introduction

Historically, attempts to explain the physics of energy and momentum input from wind to waves date back to the early twentieth century, when Jeffreys (1924, 1925) introduced the idea of airflow separation over the profile of wind waves. Potential theory predicts pressure fluctuations in the airflow, induced by the presence of surface waves, to be in antiphase with the waves, which would result in zero average energy or momentum flux across the water surface (e.g., see Young 1999). The Jeffreys airflow separation hypothesis would cause a phase shift of the pressure relative to the water surface wave and therefore provide a mechanism for positive flux from the wind to the waves if the

---

Corresponding author address: Alexander Babanin, Engineering and Industrial Sciences, Swinburne University of Technology, P.O. Box 218, Hawthorn, VIC 3122, Australia.
E-mail: ababanin@groupwise.swin.edu.au

phase shift leads to the pressure maximum occurring on the windward face of the wave. However, experiments by Stanton et al. (1932), Motzfeld (1937), and Thijsse (1951), in which the wind was blown over smooth solid waves, showed the sheltering effect to be too small to explain the observed wave growth rates. Stimulated by a review (Ursell 1956) pointing out the sorry state of our understanding of the process of wave amplification by wind, Miles devised a theory (Miles 1957, 1959, 1960) that provided an alternative mechanism of wave generation due to wave-induced slope-coherent air pressure perturbations near the surface and further contributed to the disrepute of the separation model. Janssen (1991) modified the Miles theory to allow for effects, imposed by the wave spectrum on the shape of the near-surface atmospheric boundary layer, that are critical for the determination of the growth rates by this theory. The Miles theory, with these modifications, has since been the most generally used and widely accepted mechanism to explain the amplification of existing waves under wind forcing.

In the experiment reported in this paper, we did not rely on the Miles or any other theory, or on any other experiment, for interpretation of our data and to obtain the parameterization of the wind input spectral function in terms of wind-wave properties. Furthermore, the main new features of the wind input discovered in the present study—the dependence of the dimensionless growth rates on wave steepness and flow separation—are not reproduced by any of the existing theories of wave amplification by wind and have not been previously observed in experiments. We have, however, included a brief review of the main theories and experiments that were dedicated to wave generation by wind to emphasize the incomplete and often contradictory state of knowledge in this field.

Several experimental studies have been undertaken to test the Miles theory. The most sophisticated so far—the Bight of Abaco experiment (Snyder et al. 1981)—gave temporal growth rates

$$\gamma = \frac{\rho_w}{\rho_a}\frac{1}{\omega E(\omega)}\frac{\partial E(\omega)}{\partial t} \qquad (1)$$

of

$$\gamma = (0.2 - 0.3)(U_5/c - 1), \qquad (2)$$

in reasonable accord with Miles's theoretical conclusions (see also Plant 1982; Young 1999). Here $E(\omega)$ is the radian frequency (ω) spectrum of wave energy, ρ_ω and ρ_a are the water and air density, respectively, U_5 is the wind speed at 5-m height, and c is the phase speed of wave propagation.

The relation of γ to the growth-rate parameters ζ, introduced by Miles (1957), and β, introduced by Hasselmann (1960), is as follows:

$$\gamma = \frac{\rho_w}{\rho_a}\zeta = \frac{\rho_w}{\rho_a}\frac{1}{\omega}\beta. \qquad (3)$$

Plant (1982) summarized results of many previous observations and his resulting dependence

$$\beta = \frac{(0.04 \pm 0.02)u_*^2\omega\cos\theta}{c^2} \qquad (4)$$

(where u_* is friction velocity) agrees in general with theory as proposed by Miles (1959) and Janssen (1991), subject to significant data scatter. At some values of u_*/c the measured values of β varied by an order of magnitude.

A few further attempts to investigate the atmospheric input included both field and laboratory experiments. Here, we mention experiments by Hsiao and Shemdin (1983), Hasselmann and Bösenberg (1991), Donelan (1999), among others. Hsiao and Shemdin collected data over the range of inverse wave ages $1 < U_{10}/c < 7.4$, extending the Snyder et al. (1981) range, $1 < U_{10}/c < 3$, and found a quadratic dependence of γ on U_{10}/c:

$$\gamma = 0.12(U_{10}/c - 1)^2. \qquad (5)$$

Relation (5) gives significantly smaller values of the growth rates than (2) for mature wave conditions comparable to those of the Bight of Abaco experiment.

Hasselmann and Bösenberg (1991) used the North Sea field experiment data and produced results almost identical to those of Snyder et al. (1981):

$$\gamma = (0.25 \pm 0.07)(U_5/c - 1). \qquad (6)$$

Nevertheless, the Miles theory has never been proven beyond reasonable doubt. Also, the theory has obvious limitations and, therefore, cannot be the only mechanism responsible for wind–wave interactions. For example, for an adverse wind, classical Miles theory results in no interaction between wind and waves because a critical height does not exist for such situations [Miles's (1993) revisit of the wave generation issue showed that there is some attenuation in such circumstances due to turbulent diffusion, but damping rates are small]. However, in a laboratory experiment Donelan (1999) showed that waves are strongly attenuated in an adverse wind, thereby demonstrating that the Miles theory is not relevant to this case:

$$\gamma = \begin{cases} 0.28(U_{\lambda/2}/c - 1)|U_{\lambda/2}/c - 1| & \text{for} \quad U_{\lambda/2}/c - 1 \geq 0 \\ 0.11(U_{\lambda/2}/c - 1)|U_{\lambda/2}/c - 1| & \text{for} \quad U_{\lambda/2}/c - 1 < 0, \end{cases} \tag{7}$$

where $U_{\lambda/2}$ is the wind velocity at $\lambda/2$; that is, at a height of one-half of the wavelength λ.

On the other hand, there is definite experimental evidence in favor of the Miles theory. Hristov et al. (2003), in a carefully designed field experiment revealed peculiarities of velocity behavior in phase and amplitude that can be attributed to critical layer effects. Thus, the general applicability of the Miles theory to the wind–wave interaction problem remains unresolved: effects predicted by Miles are confirmed experimentally, but also there are experimental effects that cannot be explained within the framework of Miles's approach.

The Miles theory is linear and quasi-laminar: turbulence is only considered to be important to establish the vertical profile of wind shear. There are several alternatives to this theory that are nonlinear and fully turbulent. Stewart (1967), Longuet-Higgins (1969), Sykes (1980), Jacobs (1987), Zeman and Jenssen (1987), van Duin and Janssen (1992), among others, contributed to these efforts. The most systematic fully turbulent approach resulted in the two-layer theory by Townsend (1980) and Belcher and Hunt (1993), hereinafter referred to as the TBH theory.

TBH theory investigated the behavior of fully turbulent boundary layers in the presence of a two-dimensional propagating wave. In what they term the inner layer (IL—the near-surface part of the boundary layer) perturbations of the turbulent shear stresses are principally important as they are asymmetric along the wave profile and therefore lead to amplification of the wave. Thus, if Miles's critical layer lies within the inner layer, its singular behavior is strongly suppressed by the turbulence and such quasi-laminar theories become inappropriate. However, there are analytical indications that the inner layer is much thinner than follows from TBH and numerical simulations described below (Beljaars and Taylor 1989; Walmsley and Taylor 1996).

The simulations by Kudryavtsev et al. (2001, Fig. 1) showed that the critical height almost always lies within the IL. Only for $U_k/c_p \sim 1$ (U_k is the wind speed at k^{-1} height, where $k = 2\pi/\lambda$ is the wavenumber for frequency ω) will the critical height be outside the IL, allowing for the Miles mechanism to work on waves of corresponding scales k and ω. These waves are usually long, at least for open-ocean conditions, and perhaps these are the waves on which Hristov et al. (2003) measured the Miles effect from the Research Platform (R/P) *Floating Instrument Platform* (*FLIP*). For such waves, however, the critical height is large and consequently the curvature of the vertical wind profile is small, leading to low energy transfer rates due to the Miles (1957, 1959, 1960) mechanism. On the other hand, the lower limit of the range $c/u_* = 16$–40 in Hristov et al. (2003) was limited by the measurement height, and if the effect persists into the younger wave seas (which we do not know) that would support the relative importance of the Miles mechanism across a wider range of scales and air–sea conditions.

Thus, if TBH theory is valid, the Miles mechanism works in addition to other mechanisms and can exhibit itself in field measurements, but its efficiency is small in general, and vice versa: if the Miles mechanism is shown to work across a broad range of conditions and wave scales, that would limit the scope of potential application of TBH theory. Thus, TBH theory is a further step in the direction of representing the turbulence, but does it explain wind–wave interaction in the general case?

The answer is not certain. For example, in adverse winds where the Miles theory does not produce wind–wave interaction, the Belcher and Hunt (1993) mechanism tends to attenuate the wave motion. They conclude that the wave amplitude in counterflow attenuates faster than it increases in coflow cases. This conclusion is applicable for slow waves, and for fast waves Belcher and Hunt (1998) further conclude that the time scale for damping fast waves is much longer than the time scale for growth of slow waves and, therefore, the fast waves interact only weakly with wind.

This is, however, in contradiction with the laboratory observation by Donelan (1999) who showed [Eq. (7)] that negative growth rates for the adverse wind are smaller by a factor of 2½ than those for the favorable wind. However, it produces damping rates larger than growth rates, for comparable wind forcing U/c, for fast waves and otherwise for slow waves. More recently, Peirson et al. (2003) reported the attenuation rates of slow waves by opposing wind greater than those of both experiment and theory. Their explanation, that the excessive counterwind wave attenuation is due to interactions between waves and the wind-induced currents or near surface water turbulence, is beyond the scope of the present paper.

One can speculate, perhaps, that a few coupling mechanisms may be jointly pumping energy into the following waves (Belcher and Hunt 1998), whereas in the absence of flow separation only the orbital velocity effects of Belcher and Hunt can remove it from opposing waves. Also, it is not at all clear whether subtle TBH effects associated with asymmetrical perturbations of Reynolds stresses, close to the surface of a symmetrical monochromatic two-dimensional wave, will apply more generally for a full directional wave spectrum. Nonetheless, the distortion of the streamlines leading to a shift of the pressure maximum from the trough to the windward face of the wave is referred to as "nonseparated sheltering" and is quadratic in the ratio of wind speed to wave phase speed.

Furthermore, wave breaking causes airflow separation and Jeffreys-like phase shifts between the pressure and the underlying wave surface (Banner and Melville 1976; Banner 1990; Kudryavtsev and Makin 2001; Makin and Kudryavtsev 2002). This effect does not, of course, take place before the waves have been established and start breaking but, once they are, a large increase (typically 100%) in the total wind stress is observed for breaking waves (Banner 1990), which may support up to 50% of the total wave-induced stress (Kudryavtsev and Makin 2001). Since wave breaking can be very frequent (Babanin et al. 2001), the breaking-induced separation can result in noticeable enhancement of the atmospheric input to the waves (Young and Babanin 2001). The enhancement of the wind input due to wave breaking will be the subject of another paper on the results of this study that is being prepared by the authors and that will hereinafter be referred to as Part III.

Therefore, neither quasi-laminar nor fully turbulent theories seem capable of accommodating all observed experimental wind–wave interaction effects. On the contrary, the observed effects are not inconsistent with either of the theories. In this paper we examine the growth rates in the parametric space suggested by the sheltering (separated or not) idea of Jeffreys.

Many other effects can contribute significantly to wave growth. Gustiness of the wind, which is always a feature of real wind fields, is accommodated in a number of theories (Janssen 1986; Nikolaeva and Tsimring 1986; Miles and Ierley 1998, among others) and may result in either reduction of the energy transfer or its enhancement, of up to an order of magnitude compared to predictions of Miles theory. Numerical simulation of the influence of gustiness has shown that up to 30%–40% increase in the average wave height can be expected after these effects are included (Abdalla and Cavaleri 2002).

The waves are also nonstationary, which has been shown to have a major effect on estimating the wind input. Uz et al. (2002) concluded that the wind stress, that is, momentum transfer between air and water, tends to be higher with decreasing wind than with increasing wind at a given wind speed, mainly due to delayed response of the short waves to varying wind forcing. Skafel and Donelan (1997) demonstrated modulation of the wind stress by the passage of wave groups. Agnon et al. (2005) found finescale correlated inhomogeneity of the wind–wave energy input and wave skewness and asymmetry. At shorter scales of dominant waves, Kudryavtsev and Makin (2002) and Hara and Belcher (2002) suggested different mechanisms of modulation of the surface roughness, due to the longer waves. Effects of the nonstationarity on variations of the drag coefficient have also been shown by Rieder (1997) and Drennan et al. (1999). Numerical models of wave growth assuming constant roughness underestimate the growth rate parameter by a factor of 2–3 when compared with measured values.

Another indicator of the relative efficiency of wind–wave interaction in favorable or adverse winds comes from stress measurements when swell is present on the ocean surface. Dobson et al. (1994) did not find noticeable influence of the swell on the sea drag, whereas Donelan et al. (1997), Drennan et al. (1999), and Larsen et al. (2003) revealed significantly enhanced drag coefficients for cross-wind swell and, particularly, for adverse-to-the-wind swell. Smedman et al. (1999), Drennan et al. (1999), Grachev and Fairall (2001), and Grachev et al. (2003) observed negative stress, which is ascribed to the momentum flux from the waves to the wind or swell outrunning the wind. However, evidence for such enhanced or negative wave-induced stress is indirect since no wave-induced motion has been directly identified in the wind flow in those experiments.

A new feature of air–sea interaction at strong winds was discovered by Donelan et al. (2004) in a laboratory experiment. They showed that the aerodynamic roughness has a limiting value in strong winds. This result, along with the full separation effect found in the present paper, point to an important, but not completely unexpected, conclusion. The drag coefficient dependences obtained at moderate wind conditions and then extrapolated into strong-wind situations may significantly overestimate the drag and air–sea momentum exchange.

To summarize this brief review of wind–wave coupling theory, we conclude that, to date, no fully consistent and conclusive theory of wave generation by wind exists. Suggested theoretical mechanisms need further elaboration and detailed empirical verifications, particularly as they are sometimes incompatible. Problems associated with experimental validation of wave generation theories are further complicated by the fact that a number of additional phenomena alter the wind–wave coupling in a very significant manner.

Existing experimental data, on the other hand, do not provide the necessary accuracy and insights either. As has been mentioned above, measured nondimensional growth rates are scattered by an order of magnitude and the parameterizations result in estimates that can differ by more than 100% [see Eqs. (2)–(7)]. Yet, these parameterizations form the basis of the wind input source function used in contemporary wave models.

Despite the apparent need for improvement of the wind input source function in modeling and predicting wave evolution, only a handful of experimental studies have been undertaken so far to directly measure spectral distribution of energy and momentum transfer from the wind to the waves and associated wave growth rates. This is due largely to the complexity of the phenomenon and the extreme technical and physical difficulties of making measurements of wave-coherent pressure and velocity pulsations very close to the surface using rapidly moving and accelerated probes (Donelan et al. 2005).

Partly to address the general questions raised above and partly in an attempt to parameterize the wind input function for waves under shoaling and strongly wind-forced conditions, a new field experiment was undertaken to study the wind–wave coupling and other source functions at Lake George, New South Wales, Australia, in 1997–2000 (Young et al. 2005). The main part of the wind input measurements was done during the Australian Shallow Water Experiment (AUSWEX) in August–September 1999 when a high-precision wave-follower system, developed at the University of Miami was deployed. The principal sensing hardware included Elliott pressure probes (Elliott 1972), hot film anemometers, and Pitot tubes. The wave follower recordings were supplemented by a complete set of relevant measurements in the atmospheric boundary layer, on the surface of the lakes, and in the water body. The technical details of the boundary layer study are described in detail in Part I of this work (Donelan et al. 2005). Here, in Part II, we will investigate the physics of the energy transfer to develop a parameterization suitable for use in spectral wave models. Part III will further detail the parameterization to account for effects of wind input enhancement due to wave breaking.

In section 2 we discuss the problem of extrapolating the pressure, measured at a certain height above moving waves, down to the water surface where the wind–wave coupling occurs. This is a crucial problem for experimental studies of the boundary layer since most in situ measurement technologies are not capable of sensing the pressure and velocity directly at the wavy surface and, therefore, have to rely on extrapolations. The full separation hypothesis is discussed in section 3. Section 4 describes the main results of the paper: a parameterization of the spectral function of wind input in terms of the properties of the wind profile and the wave field. Section 5 demonstrates a way to reconcile previously obtained and scattered growth rate estimates and their parameterizations, shows results of spectral measurements of the wind input, and provides cross-validations. In section 6, our conclusions are summarized and directions for further investigations are outlined.

2. Measurement of the wave-induced pressure and wind-input spectral functions

The measurement procedure for the wave-induced pressure and data analysis used to obtain the wind-input spectral functions is described in detail in Donelan et al. (2005). Here, we outline briefly the main points of the analysis routine and concentrate on the important issue of extrapolating the pressure, measured at some height above the passing waves, down to the moving water surface.

a. Data analysis

It is known that the component of pressure that is correlated with the water surface slope or, as it is often termed, the component of pressure in quadrature with the water surface will result in an energy flux from the wind to the waves (see, e.g., Donelan 1999; Young 1999):

$$\frac{1}{2}\frac{\partial a^2(\omega)}{\partial t} = \frac{1}{\rho_w g} I(\omega) = \frac{1}{\rho_w g} \overline{p\frac{\partial \eta}{\partial x}} c(\omega) = \frac{1}{\rho_w g} \overline{p\frac{\partial \eta}{\partial t}}. \tag{8}$$

Here ω is the angular frequency, $I(\omega)$ is the corresponding one-dimensional frequency function of the wind energy input, g is the gravitational constant, $p(x, t)$ is the pressure exerted by the air on the surface, $\eta(x, t) = a \cos(kx - \omega t)$ is the surface elevation of amplitude $a(\omega)$ at distance x and time t, and k is the wavenumber. The overbar represents an average with respect to time.

The nondimensional growth rate is customarily expressed in terms of the fractional energy increase per radian, $\zeta = (\rho_a/\rho_w)\gamma$ [defined previously in Eq. (1)], which is a spectral function:

$$\zeta(\omega) = \frac{\rho_a}{\rho_w}\gamma(\omega) = \frac{1}{\omega E(\omega)}\frac{\partial E(\omega)}{\partial t}, \tag{9}$$

where $E(\omega)$ is the spectrum of surface elevation. Equations (8) and (9) lead to (Snyder et al. 1981)

$$\gamma(\omega) = \frac{Q(w)}{\rho_a g E(\omega)}, \tag{10}$$

where

$$Q(\omega) = \langle p(\omega)\eta(\omega)^*\rangle \tag{11}$$

is the quadrature spectrum between the wind-induced pressure p and the surface elevation η, the angle brackets denote ensemble averaging in Fourier space, and the asterisk refers to the complex conjugate.

As far as direct experimental measurements of the wind input are concerned, the goal is to accurately estimate the quadrature spectrum $Q(\omega)$ based on simultaneous recordings of the surface elevation and the surface pressure. In the present study, the input function properties will be routinely interpreted in terms of the nondimensional ratio, $\gamma(\omega)$ as described by (10). Once the growth rate function $\gamma(\omega)$ is known and the power spectrum $E(\omega)$ is available, the dimensional spectral wind energy input is

$$I(\omega) = \rho_a \omega g \gamma(\omega) E(\omega). \tag{12}$$

The wind momentum input spectrum $M(\omega)$ is

$$M(\omega) = I(\omega)/c(\omega) = \rho_a k g \gamma(\omega) E(\omega), \tag{13}$$

and

$$\int_\omega M(\omega)\, d\omega = \tau^w, \tag{14}$$

where τ^w is the wave-induced component of the wind stress.

b. Height decay of the wave-induced pressure

As indicated above, pressure $p(x, t)$ in all relevant formulas in section 2a is the pressure exerted by the air at the water surface. In real experiments with open air sensors however, the pressure is never measured at the water surface itself, but at some height z above it. The wave-induced pressure, which is one of the two main components of the quadrature spectrum (11), decays rapidly away from the wavy surface.

Potential flow theory predicts exponential decay for the wave-induced pressure:

$$p(z) = p_0 \exp(-\alpha k z), \tag{15}$$

where p_0 is the surface pressure and $\alpha = 1$. This profile (15) has never been validated experimentally, and there are accounts of deviations from this profile. For example, Elliott (1972), based on his field measurement data, suggested that away from the mean surface the wave-induced air pressure decays essentially exponentially, but the decay is less rapid than that predicted by potential flow theory.

Depending on the height of the pressure probe, such differences can lead to very significant discrepancies if the pressure measurements are extrapolated down to the surface in order to estimate the quadrature spectrum (11). The two exponential profiles, $\exp(-kz)$ and $\exp(-0.75kz)$ are compared in Fig. 1 for the peak frequency wave scale of record LG9 (Table 1). If the measurements of p were taken at $z = 0.1$ m above the water (Fig. 1a), the two extrapolations would result in 5% difference for p_0 but, if the measurement height was $z = 0.5$ (Fig. 1b), the difference would represent a 27% difference for p_0.

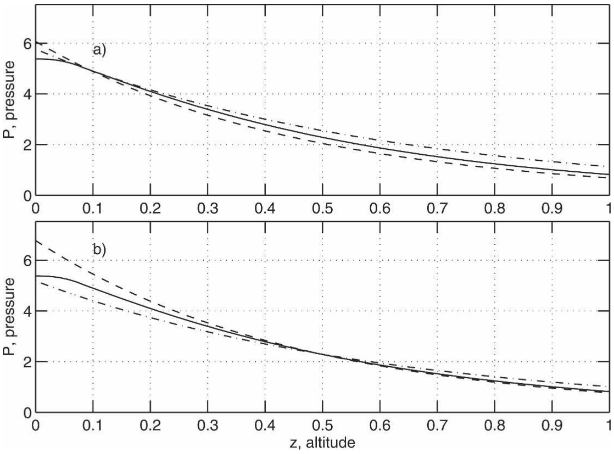

FIG. 1. Comparison of the Kudryavtsev et al. (2001) pressure profile (solid line) with exponential decays: $\exp(-kz)$ (dashed line) and $\exp(-0.75kz)$ (dash–dotted line). Estimations of the profiles are made for $U_{10} = 12$ m s^{-1}, $u_* = 0.45$ m s^{-1}, and frequency $f = 0.55$ Hz (record LG9, Table 1) assuming that the measurements are conducted at (a) $z = 0.1$ m and (b) $z = 0.5$ m.

We note here that, since potential flow theory is not capable of describing wind–wave interaction in the first place, the validity of its other conclusions regarding wave-induced perturbations is not obvious either. This pertains to the height decay of the wave-induced pressure. The proposed wind generation mechanisms, which alter the structure of the potential flow over the waves, might well modify the pressure decay with altitude.

The pressure amplitude vertical profile $p(z)$ [given by Eq. (15)], predicted by potential theory for a particular scale k, only depends on the magnitude p_0 of the pressure, induced at the surface by waves of the same scale. Kudryavtsev et al. (2001), based on TBH theory, concluded that the wave-induced pressure profile, correlated with the wave slope, should depend on an integral of the wind profile in the boundary layer rather than on the surface pressure p_0 alone.

The TBH perturbations of the turbulent shear stresses along the wave profile within the IL produce an imaginary part of the horizontal velocity fluctuations (fluctuations in quadrature with the wavy surface) that, as a result of the continuity principle, generates a real part of the vertical velocity (fluctuations in phase with the waves). The latter penetrates into the outer layer (OL) and generates the slope-correlated pressure,

TABLE 1. Summary of AUSWEX records used in the wind input study: U_{10} is the wind speed at 10 m height, u_* is the friction velocity, f_p and c_p are the peak frequency and phase speed, respectively, d is the water depth at the measurement location, and h is the height of Elliott pressure probe above the water level (in case of the fixed mode, this is the height above the mean water level).

Record	U_{10} (m s^{-1})	u_* (m s^{-1})	f_p (Hz)	H_s (m)	d (m)	U_{10}/c_p	h (m)	Mode
LG8	11.9	0.44	0.54	0.156	0.319	7.2	0.021	Following
LG9	12.0	0.45	0.55	0.134	0.286	7.6	0.042	Following
LG10	8.1	0.30	0.76	0.076	0.329	5.2	0.149	Following
LG11	10.6	0.45	0.57	0.078	0.315	6.5	0.256	Following
LG12	9.2	0.27	0.67	0.065	0.263	6.3	0.370	Fixed
LG13	8.2	0.35	0.62	0.055	0.279	5.3	0.254	Fixed
LG14	7.1	0.30	1.14	0.061	0.270	5.7	0.191	Following
LG15	7.3	0.31	0.60	0.065	0.276	4.8	0.202	Following
LG16	7.4	0.31	0.81	0.065	0.287	5.1	0.291	Following
LG17	7.3	0.28	0.86	0.074	0.254	5.3	0.194	Following
LG18	9.5	0.30	0.83	0.070	0.272	6.7	0.288	Following
LG19	8.9	0.30	0.64	0.092	0.231	6.3	0.302	Fixed
LG20	8.9	0.32	0.79	0.100	0.238	6.5	0.195	Fixed
LG21	9.0	0.34	0.86	0.106	0.216	6.9	0.167	Fixed
LG22	8.6	0.31	0.66	0.087	0.240	6.0	0.143	Fixed
LG23	8.5	0.32	0.67	0.068	0.249	5.9	0.384	Fixed

which in turn is impressed on the IL and produces an energy flux to the waves.

The algorithm, provided to us by Kudryavtsev for computation of the pressure profile (hereinafter KMM), reads:

$$p(z) = \int_z^\infty \mathrm{Re}[w(z)][U(z) - c]\, d(kz), \tag{16}$$

where $w(z)$ is the profile of the vertical velocity perturbation, the real part of which is correlated with the wave elevation and produces the slope-correlated variation of the air pressure:

$$\mathrm{Re}[(w(z)] = \exp(-kz) \int_{z_0}^{z} \mathrm{Im}[(u_0(z)]\, dz \tag{17}$$

and u_0 is the zeroth-order solution for the horizontal velocity perturbation:

$$\mathrm{Im}(u_0) = \begin{cases} \ln(z/z_0) & \text{for} \quad z < nl \\ 0 & \text{for} \quad z \geq nl. \end{cases} \tag{18}$$

Here nl is the height of the IL, while l is the IL scale:

$$kl = \frac{2\kappa u_*}{|U(l) + c|}, \tag{19}$$

and the surface roughness z_0, friction velocity u, and von Kármán constant $\kappa = 0.42$ are the parameters of the mean wind velocity logarithmic profile $U(z) = (u_*/\kappa)[\ln(z/z_0)]$. It is accepted that $n \approx 2$ for $U/c > 1$ waves and $l \sim 0.1/k$ for a broad range of conditions.

The KMM model pressure profile is shown in the panels of Fig. 1. It deviates significantly from the exponential profile and, if used to extrapolate the measured pressure down to the water surface, can produce values of surface pressure p_0 quite different from those predicted by extrapolations based on (15). The difference will depend on the height of pressure measurements. If measured relatively high above the water level, the pressure profile will not depart significantly from exponential, and the difference will probably be hard to discern experimentally. Closer to the surface, however, the difference can become significant. For the conditions of record LG9 (Table 1), if the measurements of p were made at $z = 0.1$ m above the water (Fig. 1a), the KMM extrapolations would give surface pressure levels p_0 smaller than either of the two exponents but, if the measurement height was $z = 0.5$ (Fig. 1b), the KMM value of p_0 would fall between the extrapolations based on $\exp(kz)$ and $\exp(0.75kz)$. Therefore, the KMM profile is not merely a systematic shift relative to the exponential profile, but a qualitatively different result that can provide values of the surface pressure both greater and less than those provided by the exponential extrapolation, depending on the wind profile. Experimental verification of the KMM profile is difficult, however, since significant deviations from exponential profiles should only be observed very close to the surface.

A potential advantage of the KMM profile, relative to the exponential profile, is based on the fact that TBH theory, unlike potential theory, is capable of predicting both positive and negative energy and momentum exchange between the wind and the waves. Therefore its conclusions regarding behavior of the boundary layer in the immediate vicinity of the wavy water surface appear more realistic.

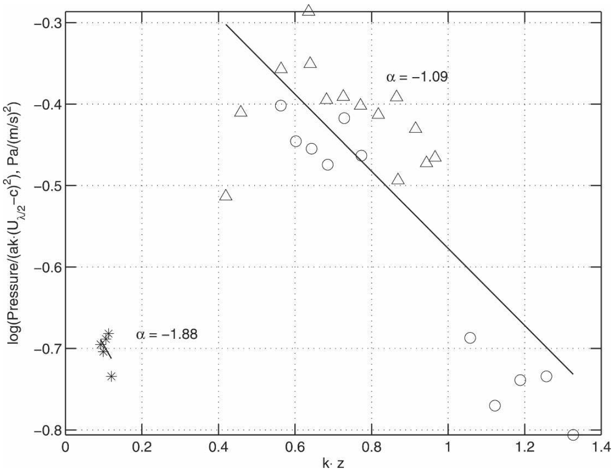

FIG. 2. Dependence of the logarithm of normalized pressure p_{norm} on the relative measurement height kz. Two clusters of data are seen, corresponding to exponential decays of $\exp(-1.88kz)$ and $\exp(-1.09kz)$. The symbols correspond to the symbol groups in Fig. 6.

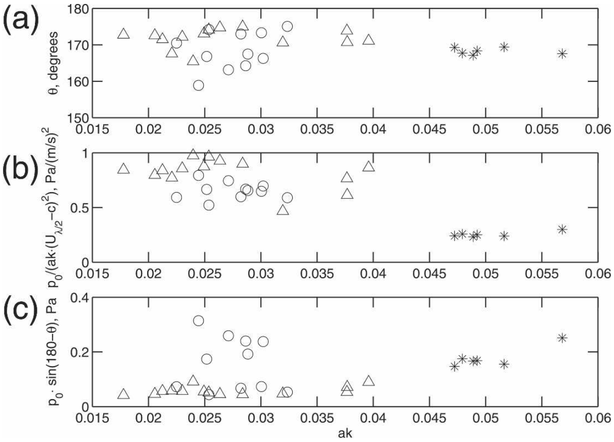

FIG. 3. Dependence of (a) phase shift, (b) normalized pressure, and (c) net momentum impact on the wave steepness. The symbols correspond to the symbol groups in Fig. 6.

The KMM profile was used extensively in the present study and has consistently produced results better than the exponential profiles, in terms of the scatter of extrapolated surface pressure values. A new feature, however, was found for the pressure decay with height during the strong wind-forcing conditions that occurred at Lake George (see section 3). A few records demonstrated airflow separation for such winds over steep waves. For these records, the KMM notion of inner and outer layers is not feasible, and for consistency we applied exponential profiles in both circumstances (as seen in Fig. 2). It is worth mentioning at this point that our pressure measurements were carried out so close to the surface that the differences between the extrapolation choices were very small.

3. Full separation

The measured height dependence of normalized pressure is graphed in Fig. 2. Since the variation of dimensionless height kz at Lake George is mainly achieved by variation of the wavenumber k, laboratory data (see the appendix) were processed to validate the wavenumber variation against variation of the measurement height z. It was concluded that, up to $\sim 1.5f_p$, both definitions of the dimensionless height provide similar exponential decay slopes, and therefore Lake George data from this frequency range were used in further analysis below.

The data separates into two classes corresponding to strong winds ($U_{10} > 11.7$ m s^{-1}) and moderate winds ($U_{10} < 10.8$ m s^{-1}), the significance of the three groups of symbols will be explained later in Fig. 6. Both classes exhibit an exponential decay but, while the lighter wind case is roughly consistent with the decay rate expected in potential flow ($\alpha = -1.09$), the strong wind cases show a much more rapid decay ($\alpha = -1.88$). The corresponding forcing rates (U/c_p) for these two flow regime cases do not group into classes but instead form a continuum roughly related to the wind speed. On the basis of evidence presented below, we believe that the quite different height dependence of the pressure is related to the character of the flow over these bottom-limited steep waves vis-a-vis the extent of flow separation. We define full separation of the flow over a steep wave crest to mean that the streamlines detach from the flow at the steep crest and do not reattach until well up the windward face of the preceding wave toward its crest. The consequence of this is that the shear layer, which is normally attached to the surface, moves upward leaving a "dead zone" in the trough between crests. Thus the external flow skips over the wave troughs and the imposed pressure pattern is weaker than in the case with nonseparated flow. However, the phase shift of the pressure maximum toward the reattachment point on the windward face of the wave becomes bigger, and it is not obvious whether the combined effect will cause enhancement or reduction of the dimensionless wave growth (10). In the fully separated case the vertical gradient of pressure would be expected to be more rapid than in the nonseparated case. In any event, the measured $p(z)$ is corrected to the surface using the observed height dependence of p.

In Fig. 3 we examine the changes of the pressure amplitude and phase, relative to the surface elevation, as the wave steepness ak is increased (wave amplitudes

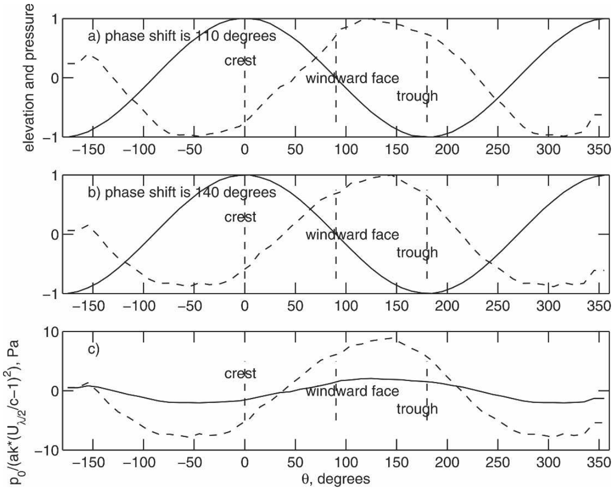

FIG. 4. Conditional (on the phase of the wave) averages of surface elevation and pressure; θ is the wave phase. Mean surface elevation profile at frequency $2f_p$ (solid line) and mean induced pressure (dashed line) for records (a) LG9 and (b) LG10 (Table 1). Surface elevations and pressure values are scaled by their respective maxima. Positions of wave crest, trough, and windward face are shown, as well as phase shift between the wave crest and pressure maximum (wave is leading). (c) The two induced pressure profiles, normalized by $ak(U_{\lambda/2}/c - 1)^2$, are compared in dimensional units. Solid line: LG9 pressure; dashed line: LG10 pressure.

a at respective wavenumbers *k* were obtained by means of the phase sampling technique described below). The phase, shown in Fig. 3a, exhibits a generally increasing departure from 180° (maximum pressure in wave troughs), moving up the windward face toward the crest of the preceding wave with increasing steepness. At the same time the pressure amplitude decreases (Fig. 3b). These are both indicators of increasingly persistent flow separation. The net momentum transfer, which is proportional to the quadrature spectrum (11), is shown in Fig. 3c. Its absolute value grows for larger steepness, which is often also associated with stronger wind-forced cases.

These flow separation effects are further demonstrated in the plots in Fig. 4, which are the average pressure conditionally sampled on the phase of the surface elevation. Phase averaging techniques have been used for a variety of applications (see, e.g., Hristov et al. 1998). Our conditional averaging method uses time series of the phase of a reference signal at a particular frequency to obtain an average profile of various flow variables sampled on the phase of the reference. For example, if the mean profile of the wave at a particular frequency is sought out of a nonfiltered wave record, the record should be bandpass-filtered in a narrow band around the chosen frequency and then used to obtain the phase time series by means of Hilbert transforms or wavelet analysis. The phase record can then be used to conditionally sample the original record to choose values of surface elevations, pressure, velocity, etc., in selected phase bins. The mean and standard deviation within the phase bins then yield the conditionally averaged flow variable on the phase of the component chosen.

Figure 4 shows these phase conditionally sampled and averaged surface elevation and pressure patterns for one of the high-wind cases (LG9, Table 1; Fig. 4a) and one of the moderate-wind cases (LG10, Table 1; Fig. 4b) at their respective double peak frequencies (i.e., $2f_p$). The solid line shows the phase-average wave profile at the frequency, and the dashed line represents the corresponding phase-average pressure distribution along the profile of this wave. Clearly, there is a significant phase shift of the pressure maximum toward the windward wave crest in both the cases as one would expect for these strongly forced waves. In case LG9, the phase shift of the pressure maximum reaches 70° relative to the wave trough, as the full separation pushes the shift farther toward the point of reattachment. The wave and pressure profiles in Figs. 4a,b are normalized by their respective maximal values for convenience of phase shift comparisons.

In Fig. 4c, the two pressure profiles are compared, normalized by steepness and Jeffrey's parameter as in Fig. 3. The amplitude of the wave-induced pressure for the fully separated case is a factor of a few smaller relative to the nonseparated case even though the wind speed, the wind forcing, and the steepness are all much higher for the former case (see Table 1). Since the streamlines flow over the separated zone in the wave trough, the fully separated induced pressure field appears to correspond to much smaller waves. This will lead to reduced momentum transfer to the waves, while the increased phase shift works in the opposite direction. Taken together the effect on the momentum transfer may be negative.

Thus, the condition of full separation, as opposed to intermittent separation or nonseparated sheltering, causes a marked change in the flow characteristics, induced surface pressure and growth rates, $\gamma(\omega)$. It therefore behooves us to attempt to determine the conditions that are conducive to full separation. The elegant laboratory experiments of Reul (1998), using particle image velocimetry to observe the streamlines over nonbreaking and spilling breakers, show distinct separation when the crest of the wave sharpens in preparation to curling over in a spilling breaker. Here the profile of the surface at the crest approaches a backward facing step and the airflow is unable to follow the surface and de-

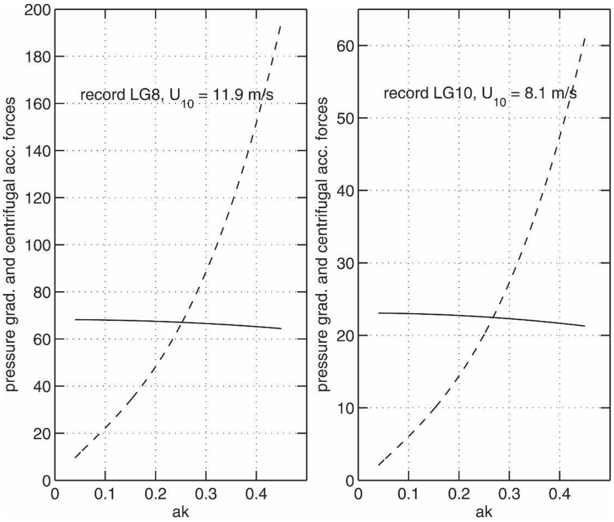

FIG. 5. Comparison of the theoretically estimated pressure gradient (solid line) and centrifugal (dashed line) forces (the estimates have units of meters per second squared). (left) LG8 record conditions (U_{10}/c_p = 7.2); in the real record 28% of waves exceed the steepness of $(ak)_{\text{threshold}}$ = 0.25. (right) LG10 record conditions (U_{10}/c_p = 5.2); in the real record 4% of waves exceed the steepness of $(ak)_{\text{threshold}}$ = 0.27.

taches near the crest to reattach on the windward face of the preceding wave.

To characterize the likelihood of flow separation at or near the crest, we consider the balance of forces there. The vertical gradient of wave-induced pressure at the crest provides the centripetal acceleration to bend the streamlines over the crest and keep them in contact with the surface. The pressure gradient increases in proportion to

$$(U_{\lambda/2} - c)^2(ak)^2,$$

while the required centripetal acceleration increases in proportion to the curvature at the crest. We use the Stokes expansion to illustrate the nonlinear relation between phase speed, curvature at the crest, and wave slope:

$$\frac{\partial^2\eta}{\partial x^2} = ak^2\left[1 + 2ak + \frac{27}{8}(ak)^2 + \frac{49}{6}(ak)^3\right]. \qquad (20)$$

Using a pressure gradient determined by the flow velocity at one-half wavelength, λ/2 and the centripetal acceleration determined from the surface curvature at the crest and the flow speed at the edge of the viscous boundary layer we compare the two (Fig. 5) as a function of slope *ak* for a high-speed run and a moderate-speed run. The intersection of the lines marks the value of *ak,* above which flow separation is likely. In the high-speed case (left panel) 28% of the measured waves

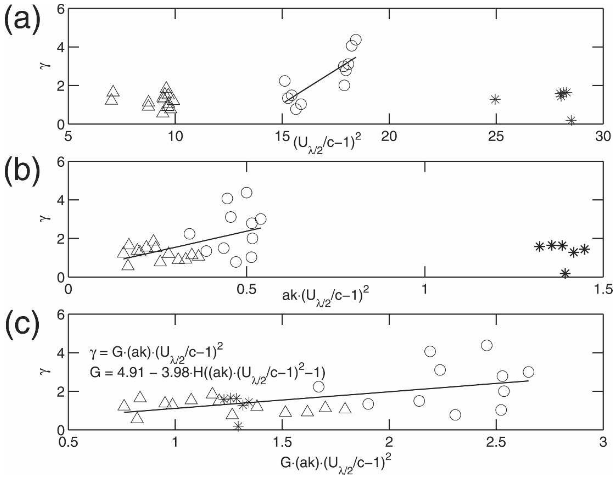

FIG. 6. Dependence of the growth rate γ on the wind–steepness parameter. (a) The wind forcing parameter is $(U_{\lambda/2}/c - 1)^2$; the data cluster in three separate groups. (b) The wind–steepness parameter is $ak(U_{\lambda/2}/c - 1)^2$; the data collapse into two groups [symbols denote the same data points as in (a)]. (c) The wind-steepness-separation parameter is $Gak(U_{\lambda/2}/c - 1)^2$; the data merge together [symbols denote the same data points as in (a)].

exceeded the threshold (ak = 0.25), while only 4% exceeded the threshold (ak = 0.27) in the moderate-wind case.

4. Parameterizing the measured growth rates

The measured growth rates, for all the cases listed in Table 1, are graphed in Fig. 6a. Most previous parameterizations of the spectral growth rates implicitly assume a concept of self-similar sheltering in which the geometry of the streamline pattern is preserved however steep the waves or strong the forcing ($U_{\lambda/2}/c$). This would lead to a linear relationship between $(U_{\lambda/2}/c - 1)^2$ and γ. The slope *s* of the relationship, $\gamma = s(U_{\lambda/2}/c - 1)^2$, is the "sheltering coefficient" and it is the product of the normalized (via the potential flow solution) pressure amplitude at the wavelength of the wave being forced and the sine of the phase shift of the pressure pattern relative to potential flow (in antiphase with surface elevation). However, as illustrated in Fig. 3, the streamline geometry does not preserve its similarity having both the shift in phase and the normalized pressure amplitude related to wave steepness. Indeed, the asymptotic value of both of these appears to approach the potential flow values of 0 and 1, respectively, as $ak \to 0$. Clearly the observed sheltering coefficients depend on *ak* and this parameter has been incorporated in Fig. 6b. The data now separate into two clusters corresponding to high winds (separation likely) and moderate winds (separation much less likely), both of which show a trend to zero growth as the abscissa tends to zero—a consequence of incorporating wave slope into the parameterization—in keeping with physical expectations. The incorporation of slope in the parameterization reflects the linear trend of phase shift (Fig. 3) with increasing slope as, we surmise, nonseparated sheltering becomes more pronounced and the streamline pattern shifts downstream with respect to the crest. On the other hand, the drop in normalized pressure amplitude signals the onset of separation, which we argue is related both to the curvature near the crest and the difference in wind speed and wave phase speed—that is, the centripetal acceleration necessary to keep the streamlines in contact with the surface. Separation occurs only when the wave-induced pressure gradient is insufficient to provide the necessary centripetal acceleration and is therefore associated with the exceedence of a threshold. As the waves are more strongly forced and become steeper, the frequency of occurrence of separation increases and the average pressure amplitude falls until all waves induce separation corresponding to some asymptotic normalized pressure amplitude. Thus we model the decreasing pressure amplitude with a function:

$$G\left[ak\left(\frac{U_{\lambda/2}}{c}-1\right)^2\right]=G(\text{arg}),\tag{21}$$

with G having a limiting value corresponding to no separation at low values of the argument:

$$G=b-q[H(\text{arg}-\text{arg}_{\text{threshold}})],\tag{22}$$

where $q = 3.98$, $b = 4.91$, and $\text{arg}_{\text{threshold}} = 1$; H is the Heaviside unit step function.

Since the growth rate γ is the product of the sine of the phase shift angle and the pressure amplitude, we model γ by

$$Gak\left(\frac{U_{\lambda/2}}{c}-1\right)^2.$$

The measured γ values are graphed versus $Gak[(U_{\lambda/2}/c)-1]^2$ in Fig. 6c. The data now fall along the regression line shown with a correlation coefficient of 0.53.

5. Discussion

To our knowledge this is the first attempt to measure the pressure growth term on waves in shallow water. The depth imposed limits on phase propagation speed have enabled us to study a wider range of forcing conditions (U/c_p) than has been possible in previous field studies. Because of the wide range of forcing we were able to explore the effect of wave steepness on nonseparated sheltering and the additional effect of full separation. Previous studies have attempted to characterize growth rates on some forcing variable such as u_*/c, $U_{\lambda/2}/c$, or U_z/c with results that show some correlation although an order of magnitude variation about the fitted curves was quite common. Although we set out to characterize growth rates in the same way, we have concluded that other variables affect the efficiency of the transfer of momentum from wind to waves and have proposed a generalized wind input that includes the effects of nonseparated sheltering and full separation. We turn our attention now to the best-known field experiments and examine their results in the light of our parameterization.

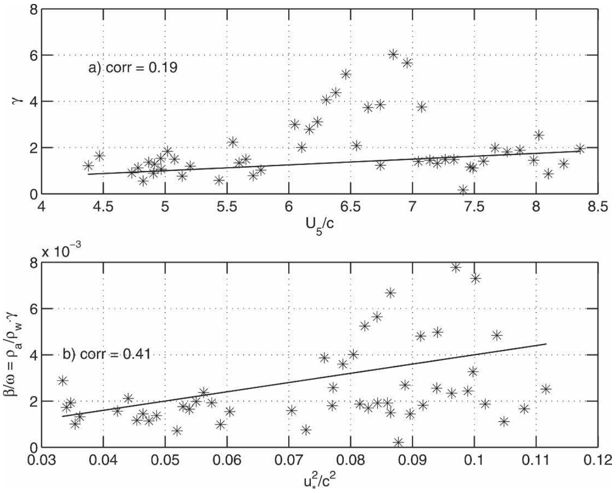

FIG. 7. Comparison of the Lake George measurement points (*) with dependences (solid lines) (a) Eq. (2) of Snyder et al. (1981) and (b) Eq. (4) of Plant (1982). The $p(z) = p_0\exp(-kz)$ extrapolation was applied to the Lake George data to obtain surface pressure values p_0 based on pressure measurements $p(z)$ at height z above the water level.

In Fig. 7, our γ values are graphed against the forcing variables used by Snyder et al. (1981) and Plant (1982): U_5/c and $(u_*/c)^2$, respectively. The lines fitted to their data are also shown. There is general agreement with the magnitudes of the data and their parameterizations, but the correlation coefficients are low: 0.19 and 0.41, respectively. In Fig. 8, hindcasting of the measurements of Donelan (1999) and Hsiao and Shemdin (1983), performed by means of the new parameterization for the values of γ at the peak of their spectra, are shown. Since amplitudes of peak waves are not known, reported significant wave height was scaled to approximately obtain peak steepness for Donelan (1999) and Hsiao and Shemdin (1983) conditions. This makes the hindcast qualitative rather than quantitative. The agreement is quite good and shows the capability of our new param-

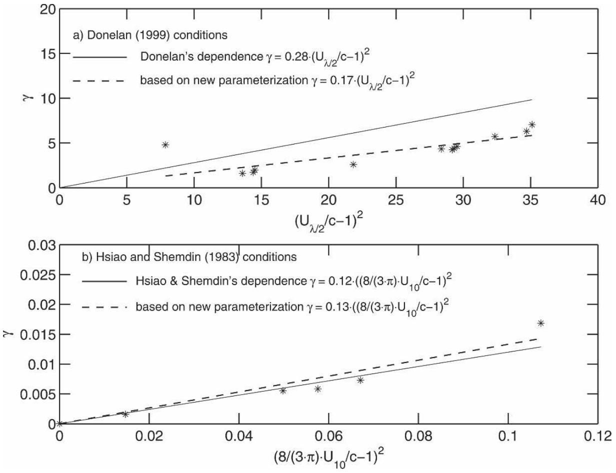

FIG. 8. Hindcast of the growth rates γ for (a) Donelan (1999) and (b) Hsiao and Shemdin (1983) conditions; the asterisk is hindcast estimates of γ at the spectral peak for the respective records, based on the parameterization (21)–(22). Solid lines: original parameterizations and dashed lines: best fit to the hindcast values of γ.

eterization to reconcile the field parameterization (5), obtained for large and old waves, and the laboratory parameterization (7), obtained for short and young waves. For these cases, the two parameterizations have sheltering coefficients differing by more than a factor of 2.

The total exchange of momentum between wind and waves serves as an integral check on the derived wind input function. Figure 9 shows the wind input measured near the spectral peak of record LG9 (solid line), while the dashed line is the computed momentum transfer to the measured wave spectrum in record LG9 using the parameterization given in section 4. The integral is calculated out to 7 Hz and is found to be 61% of the total stress as measured by hot x-film anemometry. In Fig. 10 the ratio of momentum input, measured in this way, to total stress is shown (open circles). The addition of the calculated viscous stress (skin drag) brings all the points within reasonable agreement with the hot-film estimates of total stress. This test verifies that the selected parameterization represents the measured data very well.

To make our results readily accessible for general use, we replace ak, as a measure of steepness, with the spectral saturation B_n (Banner et al. 2002)

$$B_n(\omega) = \frac{\omega^5 E(\omega)}{2g^2} A(\omega), \tag{23}$$

where A is the spectral spreading function, defined as (Babanin and Soloviev 1998)

$$A(\omega)^{-1} = \int_{-\pi}^{\pi} K(\omega, \phi)\, d\phi, \tag{24}$$

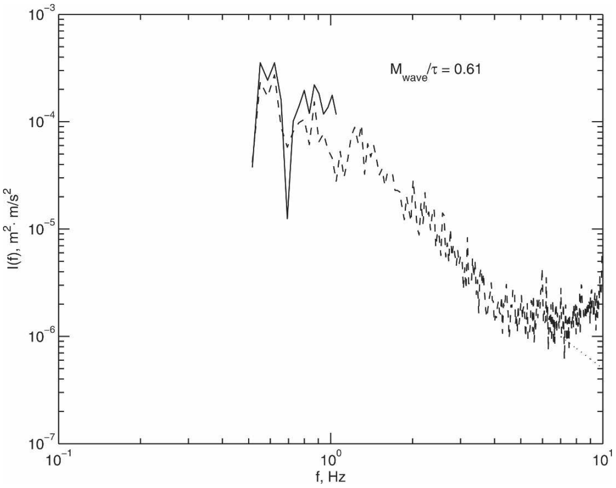

FIG. 9. Wind energy input spectral functions for the LG9 record (Table 1): measured (solid line), estimated using the (21)–(22) parameterization (dashed line), and extrapolated at higher frequencies (dotted line). Ratio of the integrated momentum flux to the wind stress τ, obtained independently by hot-wire measurements is shown.

and $K(\omega, \phi)$ is the distribution of wave spectral density at frequency ω along direction ϕ, normalized by its maximal value at this frequency:

$$K(\omega, \phi_{\max}) = 1. \tag{25}$$

The wind forcing is parameterized in terms of $U_{\lambda/2}$ as before and U_{10} also. These parameterizations are, respectively (Fig. 11),

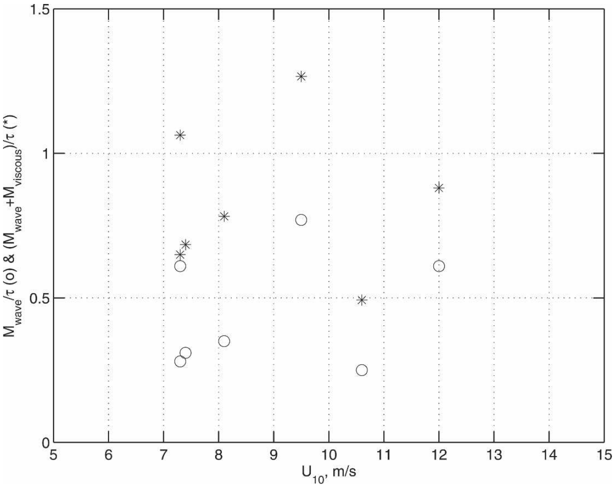

FIG. 10. Ratio of the integrated momentum flux to the wind stress τ, obtained independently by hot-wire measurements, for different LG records, (o): integrated flux consists of the integrated wave-induced stress and (*): the integrated flux is a sum of the wave-induced and estimated viscous stress.

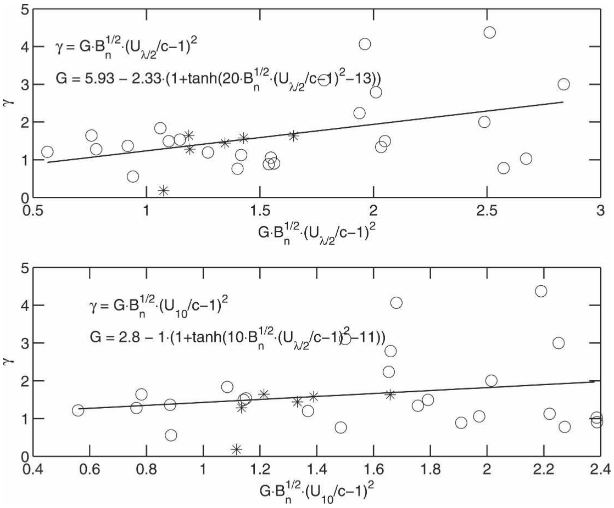

FIG. 11. Parameterizations (top) (26)–(27) and (bottom) (28)–(29) in terms of the steepness spectral analog $\sqrt{B_n}$ (23)–(24), (*): fully separated points and (o): nonseparated points.

$$\gamma = G\sqrt{B_n}\left(\frac{U_{\lambda/2}}{c} - 1\right)^2, \tag{26}$$

$$G = 5.93 - 2.33\left\{1 + \tanh\left[20\sqrt{B_n}\left(\frac{U_{\lambda/2}}{c} - 1\right)^2 - 13\right]\right\}, \tag{27}$$

and

$$\gamma = G\sqrt{B_n}\left(\frac{U_{10}}{c} - 1\right)^2, \tag{28}$$

$$G = 2.80 - 1.00\left\{1 + \tanh\left[10\sqrt{B_n}\left(\frac{U_{10}}{c} - 1\right)^2 - 11\right]\right\}. \tag{29}$$

Here, to reduce effects of the rapid changes on wave model stability, the Heaviside function was replaced by its smoothed analog, (1/2)[1 + tanh(arg)], in such a way that the experimental points in Fig. 11 are not affected.

We note here that since results on growth rate γ are based on the measurements of pressure, values of γ are omnidirectional. Therefore, the parameterization can only be used to obtain the integrated-over-direction or omnidirectional spectrum of wind input (12).

An important consequence of the parameterization is that, since $[(U/c) - 1]^2$ is a rapidly growing function of frequency ω, for virtually any steepness ak there will be a frequency $\omega_{\text{threshold}}$ for which arg = $\text{arg}_{\text{threshold}}$ in (21)–(22). Components $\omega > \omega_{\text{threshold}}$ will sustain the full separation and therefore the relative wind input at the spectral tail will go down relative to the wind input at $\omega < \omega_{\text{threshold}}$ components. This feature differs in the present parameterization from the others, which all exhibit gradual growth of $\gamma(\omega)$ toward higher frequencies. The total stress, supported by wave growth based on the current parameterization, is nevertheless consistent with the total stress measurements as demonstrated in Figs. 9 and 10.

6. Conclusions

In situ field measurements are always difficult. No matter how well the field observations are planned, the observer has no control over environmental circumstances and has to wait and hope that appropriate measurement conditions are met. Usually, no rehearsal and no replay are possible. Field instruments are typically much less sensitive and much more perturbing versions of their laboratory counterparts. Yet any theory or numerical simulation needs ultimate validation by experimental means, remote probing needs in situ verification, and laboratory results need to be tested in the field.

The Lake George experiment was designed as a field experiment with many laboratory-like characteristics. As a field site, Lake George provided significant fetches for the atmospheric boundary layer to fully adjust to the water surface and for the directional wave fields to reach bottom-limited conditions. At the same time, steady weather patterns enabled frequently repeating westerly winds at speeds of about 10 m s^{-1}. The shallowness of the lake provided multiple advantages: absence of extremely high and destructive waves, simple construction of an observational platform situated beyond the surf zone, and having walkway access. The degree of wind forcing (U/c_p) was determined by the wind speed since the phase speed of the peak was bottom-limited. In general, stronger forcing resulted in steeper waves and more breaking. In addition the relatively small scales of the waves and the availability of the platform allowed usage of laboratory versions of devices for high precision wave following and the measurements of velocity and pressure.

This all led to the successful acquisition of a dataset of direct measurements of the pressure wave growth term for very strongly forced waves, with $U_{10}/c_p = 5.1$–7.6 and U/c ranging up to 11.2, with varying wave steepness. Under such circumstances, a new feature of wind–wave interaction was revealed, which we interpreted as full separation of the airflow. Once the wave steepness and wind forcing reach the combined threshold value (22), the airflow detaches from the wavy surface downstream of the crests, skips over the troughs, and reattaches on the windward face. The effect of this is an increased shift of the phase of pressure and a marked reduction in its amplitude.

Another new feature of the pressure growth term, revealed by the Lake George study, is the dependence of the growth rates on wave steepness. It was shown that both the phase shift and the normalized induced pressure amplitude are related to the wave steepness and only approach their potential flow values as $ak \to 0$. Therefore, the effects of wave steepness were included, along with those of full separation, into the final parameterization (21)–(22). These affect the momentum transfer (form drag) in opposing ways, increasing it in moderate forcing conditions and reducing it in strong forcing conditions. The validity of the parameterization across the spectrum was verified by independent measurements of the integrated momentum flux across the interface.

The parameterization (21)–(22) is designed to work in the entire range of wave generation by wind: from light and moderate to very strong winds; from young waves to mature seas. The Lake George conditions, however, were only those of strong wind forcing. Hindcasting of available laboratory and field wave growth data was conducted, including those obtained over mature wave seas, which showed growth rates predicted by the new parameterization to agree well with the established measurements. The new parameterization was presented in a convenient form for spectral modeling (26)–(29).

It should be noted that full separation, as a new feature of air–sea interaction at small scales, needs further investigation. The Lake George dataset enabled us to parameterize the onset of the full separation effect as a switch in (22). The threshold value of $\mathrm{arg}_{\mathrm{threshold}} = 1$ is an approximate one as our nonseparated data belong to the range $\mathrm{arg} < 0.54$ and the separated ones to $\mathrm{arg} > 1.24$. It is probable that the transition to full separation is more gradual. However, we do not expect that introduction of a less rapid transition from nonseparated to fully separated airflow conditions will significantly alter wave growth rates predicted by our parameterization, but it may have some impact on the stability of numerical wave generation models.

There is another feature of wind–wave interaction, which has not been addressed in the current study: that is, the influence of wave breaking on the energy exchange between the wind and the waves. In records, used to obtain the presented parameterization, wave-breaking rates were low and the breaking was checked not to have a significant overall effect on the measured growth rates. In other circumstances, however, when breaking rates are high, the effect of the wave breaking can be important, having the potential to double the wave growth. Part III of this study will be dedicated to the investigation and parameterization of the effect of wave breaking on the wind input.

Acknowledgments. The authors gratefully acknowledge the financial support of the U.S. Office of Naval Research (Grants N00014-97-1-0234 and N00014-97-1-0233) and of the Australian Research Council (Grant A00102965). We also express our gratitude to the staff of the School of Civil Engineering of the Australian Defense Force Academy for their help during AUSWEX, particularly to Michael Jones, Mary Dalton, and John MacLeod who offered highly professional and prompt responses to all urgent demands during the experiment. The authors thank Vladimir Kudryavtsev for providing a numerical algorithm for estimating the KMM pressure profile and Frederick Dobson for his careful reading of the manuscript and many useful suggestions for its improvement. We are indebted also to the referees for many valuable criticisms.

APPENDIX

Laboratory Experiment for Height Dependency on Wind Speed

The sensitivity of the estimates of surface pressure to the form of pressure decay with altitude is apparent. Field measurements in a wave-following frame at some height above the surface are most easily extrapolated to the surface if the height dependence of the pressure amplitude is also measured. In the field campaign at Lake George we were unable to explore this height dependence for given wind speeds and wave development conditions as these did not remain steady for long enough. Consequently, we will examine similar measurements in a large (100-m length) wind–wave facility (Donelan 1999) in which a series of runs was performed with varying wind speed and wave paddle conditions. For each condition a pair of runs was made at different wave-following heights.

In the runs discussed below strong winds of 10.7 m s^{-1} (at 26 cm height) generated wind–waves that were steep and frequently breaking—analogous conditions to those often found at Lake George. The peak of the windsea at a fetch of 49 m was slightly greater than 1 Hz. The duration of each run was 819.2 s and all measurements were recorded at 20 Hz. The surface elevation was sensed by a pair of capacitance wave gauges, fixed from floor to ceiling 10 cm on either side of an Elliott pressure probe. The pressure probe was mounted on a hydraulic wave-follower at selected heights. Figures A1a and A1b show the wave induced

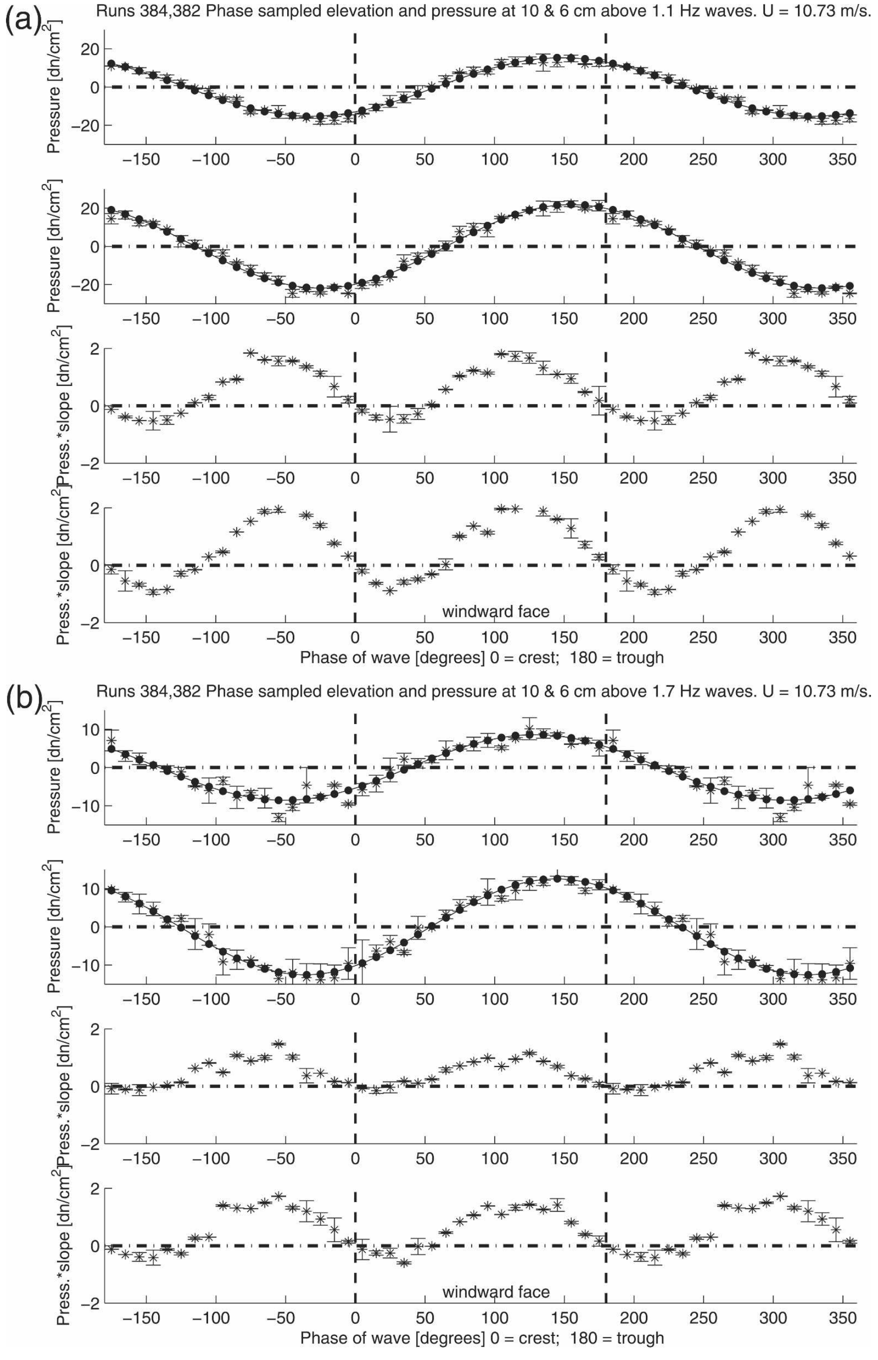

FIG. A1. (a) Phase sampled pressure at 10 and 6 cm above the water surface for 1.1-Hz waves (top two panels); corresponding momentum input to the surface (bottom two panels). (b) As in (a) but for 1.7-Hz waves.

pressure at heights of 10 and 6 cm and the corresponding momentum input to the surface calculated from the pressure–surface slope product.

The measured pressure is a combination of turbulent pressure fluctuations, p' and wave-induced fluctuations, $\tilde{p}$; the former being generally much larger than the latter. To detect the dependence of the amplitude of $\tilde{p}$ on normalized height above the surface, kz, we employ a phase-sampling procedure (see section 3) as follows: 1) bandpass the surface elevation signal to isolate the wave component of interest, $f_0 \pm \Delta f_0$; 2) apply a Hilbert transform to determine the local phase of the isolated wave component; 3) sample and average the measured pressure in 10° phase bins. These phase-sampled averages of p (i.e., $\tilde{p}$) are indicated by asterisks in the top two panels (at 10 and 6 cm height for the top and second panels, respectively). The runs are broken into two 409.6-s subruns and the error bars are plus/minus one standard deviation of the averages in each bin over the two subruns. The large dots joined by a solid line correspond to the harmonic of $\tilde{p}$ having the same frequency as the wave signal. The bottom panels are the product of the measured $\tilde{p}$ and the local slope of the wave component, assuming that the waves propagate according to the linear theory. Figure A1a is for a 1.1-Hz wave near and below the peak of the wind-generated wave spectrum, while Fig. A1b is for a 1.7-Hz component of the windsea in the "equilibrium range."

Several aspects of the induced pressure due to the waves are apparent. The pressure pattern is shifted downwind (to the left) and this is particularly evident in Fig. A1b, where the waves are relatively slow moving. The differences in centerline wind speed and phase speed are 9.34 and 9.82 m s^{-1} for Figs. A1a and A1b, respectively, and the values of kz at 10 cm and 6 cm are 0.51 and 0.31 for Fig. A1a and 1.18 and 0.71 for Fig. A1b. If the pressure amplitude falls off exponentially in kz, then the difference in amplitude would be 22% in Fig. A1a and 60% in Fig. A1b. The amplitude differences in Figs. A1a and A1b are 43% and 46%, indicating a faster than $\exp(-kz)$ fall off of the pressure amplitude in Fig. A1a and somewhat slower than $\exp(-kz)$ in Fig. A1b. The pressure amplitudes are generally larger for the longer waves on the forward face of the spectrum, although both components support about the same amount of stress because the equilibrium range waves (Fig. A1b) are steeper than those on the forward face (Fig. A1a).

On the assumption that the pressure decay with height z above a single wave component k is exponential as in Eq. (15), the exponential decay factor α may readily be obtained from the pressure amplitude measured at two heights:

$$\alpha = \ln\left[\frac{\tilde{p}(z_1)}{\tilde{p}(z_2)}\right] / k(z_2 - z_1). \tag{A1}$$

The values of α versus normalized wavenumber, k/k_p, are shown (asterisks) in Fig. A2. The estimates of α are noisy much below the peak of the amplitude spectrum (shown), but stabilize once the steepness of the wave component becomes large enough. The dashed vertical lines mark the estimates corresponding to Figs. A1a and A1b. The value of α corresponding to Fig. A1a is about 1.7, while that for Fig. A1b, on the rear face or equilibrium range of the spectrum is about 0.8. Further down the equilibrium range α continues to decrease, apparently asymptoting to a value of about 0.5. Note that the three points above the general trend at about $k/k_p = 2.2$ correspond to the second harmonic of the peak (of the slope spectrum), which will be largely bound waves rather than the free wind waves assumed in the analysis.

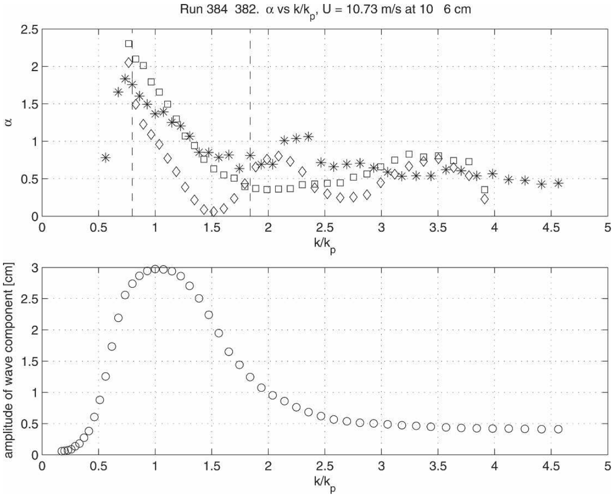

FIG. A2. (top) Values of α vs normalized wavenumber k/k_p. Asterisks: based on pressure measurements at two heights (A1) and squares and diamonds: based on measurements at a single height (A2) from the pressure measured at 6- and 10-cm height, respectively. (bottom) Amplitude of wave components at the respective wavenumbers.

In cases in which the pressure is measured at a single height above the moving surface, is there a method of estimating α? From (15) we have

$$\ln\left[\frac{\tilde{p}(z)}{\tilde{p}_0}\right] = -\alpha k z; \tag{A2}$$

Thus, the slope of the line of $\ln[\tilde{p}(z)/\tilde{p}_0]$ against kz yields an estimate of α. The dependence of p_0 on k must be known or, at least, approximated. Apart from an empirical constant, Donelan (1999) has shown a clear dependence of p_0 on $ak(U_{\lambda/2} - c)^2$; where c is the phase speed of the wave component k, $U_{\lambda/2}$ is the wind speed at one-half wavelength above it, and a is the amplitude of the component. Thus the slope of the graph of measured pressure, $p(z)$ normalized by $ak(U_{\lambda/2} - c)^2$, $\tilde{p}_N$ against kz (Fig. A3) yields the value of $\alpha(k)$. An estimate of the slope of the curves is obtained by smoothing the curves with five-point running averages (dashed

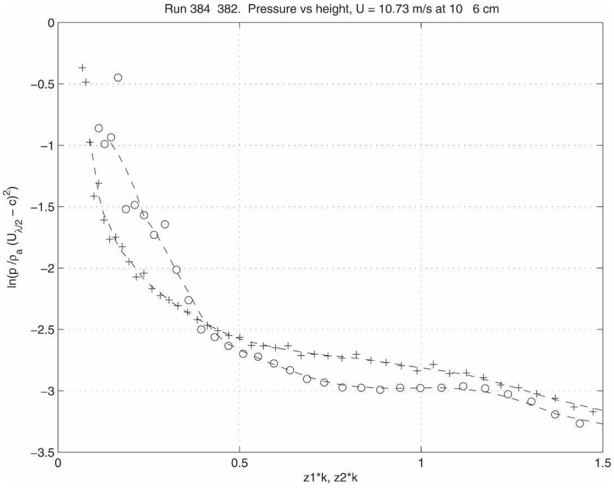

FIG. A3. Observed dependence of normalized pressure with wavenumber at fixed heights of 10 (open circles) and 6 cm (crosses); dashed lines are five-point running averages through the data points. The local slopes of these curves yield the estimates of α.

lines) and evaluating the slope at each point from $\Delta\ln(\tilde{p}_N)/\Delta kz$. These estimates of α are shown on Fig. A2 from the pressure measured at 6 and 10 cm (squares and diamonds, respectively). Near the peak and also above $2.5k_p$, the estimates of α derived in this way are in reasonable agreement with the estimates deduced from measurements at two heights (asterisks). The single height approach will be used when necessary for estimates of α near the peak. In these cases, a 20% tolerance on the value of α will be reflected in the stated uncertainty of the estimated surface pressure using (15).

REFERENCES

Abdalla, S., and L. Cavaleri, 2002: Effects of wind variability and variable air density on wave modeling. *J. Geophys. Res.,* **107,** 3080, doi:10.1029/2000JC000639.

Agnon, Y., A. B. Babanin, I. R. Young, and D. Chalikov, 2005: Fine scale inhomogeneity of wind-wave energy input, skewness and asymmetry. *Geophys. Res. Lett.,* **32,** L12603, doi:10.1029/2005GL022701.

Babanin, A. V., and Y. P. Soloviev, 1998: Variability of directional spectra of wind-generated waves, studied by means of wave staff arrays. *Mar. Freshwater Res.,* **49,** 89–101.

——, I. R. Young, and M. L. Banner, 2001: Breaking probabilities for dominant surface waves on water of finite constant depth. *J. Geophys. Res.,* **106,** 11 659–11 676.

Banner, M. L., 1990: The influence of wave breaking on the surface pressure distribution in wind-wave interactions. *J. Fluid Mech.,* **211,** 463–495.

——, and W. K. Melville, 1976: On the separation of air flow above water waves. *J. Fluid Mech.,* **77,** 825–842.

——, J. R. Gemmrich, and D. M. Farmer, 2002: Multiscale measurements of ocean wave breaking probability. *J. Phys. Oceanogr.,* **32,** 3364–3375.

Belcher, S. E., and J. C. R. Hunt, 1993: Turbulent shear flow over slowly moving waves. *J. Fluid Mech.,* **251,** 109–148.

——, and ——, 1998: Turbulent flow over hills and waves. *Annu. Rev. Fluid Mech.,* **30,** 507–538.

Beljaars, A. C. M., and P. A. Taylor, 1989: On the inner-layer scale height of boundary-layer flow over low hills. *Bound.-Layer Meteor.,* **49,** 433–438.

Dobson, F. W., S. D. Smith, and R. J. Anderson, 1994: Measuring the relationship between wind stress and sea state in the open ocean in the presence of swell. *Atmos.–Ocean,* **32,** 237–256.

Donelan, M. A., 1999: Wind-induced growth and attenuation of laboratory waves. *Wind-over-Wave Couplings. Perspective and Prospects,* S. G. Sajadi, N. H. Thomas, and J. C. R. Hunt, Eds., Clarendon Press, 183–194.

——, W. M. Drennan, and K. B. Katsaros, 1997: The air–sea momentum flux in conditions of wind, sea and swell. *J. Phys. Oceanogr.,* **27,** 2087–2099.

——, B. K. Haus, N. Reul, W. J. Plant, M. Stiassnie, H. C. Graber, O. B. Brown, and E. S. Saltzman, 2004: On the limiting aerodynamic roughness of the ocean in very strong winds. *Geophys. Res. Lett.,* **31,** L18306, doi:10.1029/2004GL019460.

——, A. V. Babanin, I. R. Young, M. L. Banner, and C. McCormick, 2005: Wave follower field measurements of the wind input spectral function. Part I: Measurements and calibrations. *J. Atmos. Oceanic Technol.,* **22,** 799–813.

Drennan, W. M., H. C. Graber, and M. A. Donelan, 1999: Evidence for the effects of swell and unsteady winds on marine wind stress. *J. Phys. Oceanogr.,* **29,** 1853–1864.

Elliott, J. A., 1972: Microscale pressure fluctuations near waves being generated by wind. *J. Fluid Mech.,* **54,** 427–448.

Grachev, A. A., and C. W. Fairall, 2001: Upward momentum transfer in the marine boundary layer. *J. Phys. Oceanogr.,* **31,** 1698–1711.

——, ——, J. E. Hare, J. B. Edson, and S. D. Miller, 2003: Wind stress vector over ocean waves. *J. Phys. Oceanogr.,* **33,** 2408–2429.

Hara, T., and S. E. Belcher, 2002: Wind forcing in the equilibrium range of wind-wave spectra. *J. Fluid Mech.,* **470,** 223–245.

Hasselmann, D., and J. Bösenberg, 1991: Field measurements of wave-induced pressure over wind-sea and swell. *J. Fluid Mech.,* **230,** 391–428.

Hasselmann, K., 1960: Grundgleichungen der Seegangsvorhersage. *Schifftechnik,* **7,** 191–195.

Hristov, T., C. Friehe, and S. Miller, 1998: Wave-coherent fields in air flow over ocean waves: Identification of cooperative behavior buried in turbulence. *Phys. Rev. Lett.,* **81,** 5245–5248.

——, S. D. Miller, and C. A. Friehe, 2003: Dynamical coupling of wind and ocean waves through wave-induced air flow. *Nature,* **422,** 55–58.

Hsiao, S. V., and O. H. Shemdin, 1983: Measurements of wind velocity and pressure with a wave follower during MARSEN. *J. Geophys. Res.,* **88,** 9841–9849.

Jacobs, S. J., 1987: An asymptotic theory for the turbulent flow over a progressive wave. *J. Fluid Mech.,* **174,** 69–80.

Janssen, P. A. E. M., 1986: On the effects of gustiness on wave growth. KNMI Afdeling Oceanografisch Research Memo 00-86-18, DeBilt, 17 pp.

——, 1991: Quasi-linear theory of wind-wave generation applied to wave forecasting. *J. Phys. Oceanogr.,* **21,** 1631–1642.

Jeffreys, H., 1924: On the formation of waves by wind. *Proc. Roy. Soc.,* **107A,** 189–206.

——, 1925: On the formation of waves by wind. II. *Proc. Roy. Soc.,* **110A,** 341–347.

Kudryavtsev, V. N., and V. K. Makin, 2001: The impact of air-flow separation on the drag of the sea surface. *Bound.-Layer Meteor.,* **98,** 155–171.

——, and ——, 2002: Coupled dynamics of short wind waves and the air flow over long surface waves. *J. Geophys. Res.,* **107,** 3209, doi:10.1029/2001JC001251.

——, ——, and J. F. Meirink, 2001: Simplified model of the air flow above the waves. *Bound.-Layer Meteor.,* **100,** 63–90.

Larsen, X. G., V. K. Makin, and A.-S. Smedman, 2003: Impact of the waves on sea drag: Measurements in the Baltic Sea and a model interpretation. *Phys. Fluids,* **12,** 97–120.

Longuet-Higgins, M. S., 1969: Action of a variable stress at the surface of water waves. *Phys. Fluids,* **12,** 737–740.

Makin, V. K., and V. N. Kudryavtsev, 2002: Impact of dominant waves on sea drag. *Bound.-Layer Meteor.,* **103,** 83–99.

Miles, J. W., 1957: On the generation of surface waves by shear flows. *J. Fluid Mech.,* **3,** 185–204.

——, 1959: On the generation of surface waves by shear flows, Part 2. *J. Fluid Mech.,* **6,** 568–582.

——, 1960: On the generation of surface waves by turbulent shear flows. *J. Fluid Mech.,* **7,** 469–478.

——, 1993: Surface wave generation revisited. *J. Fluid Mech.,* **256,** 427–441.

——, and G. Ierley, 1998: Surface-wave generation by gusty wind. *J. Fluid Mech.,* **357,** 21–28.

Motzfeld, H., 1937: Die turbulence Strömung an welligen Wanden. *Z. Agnew Math. Mech.,* **17,** 193–212.

Nikolaeva, Y. I., and L. S. Tsimring, 1986: Kinetic model of the wind generation of waves by a turbulent wind. *Izv. Atmos. Oceanic Phys.,* **22,** 102–107.

Peirson, W. L., A. W. Garcia, and S. E. Pells, 2003: Wave attenuation due to opposing wind. *J. Fluid Mech.,* **407,** 345–365.

Plant, W. J., 1982: A relationship between wind stress and wave slope. *J. Geophys. Res.,* **87,** 1961–1967.

Rieder, K. F., 1997: Analysis of sea-surface drag parameterizations in open ocean conditions. *Bound.-Layer Meteor.,* **82,** 355–377.

Reul, N., 1998: Etude expérimentale de la structure de l'écoulement d'air au-dessus de vagues courtes déferlantes. Ph.D. thesis, Universite de la Mediterranee, Aix-Marseille II, 334 pp.

Skafel, M. G., and M. A. Donelan, 1997: Laboratory measurements of stress modulation by wave groups. *Geophysica,* **33** (2), 9–14.

Smedman, A.-S., X. Högström, H. Bergström, A. Rutgersson, K. K. Kahma, and H. Pettersson, 1999: A case study of air–sea interaction during swell conditions. *J. Geophys. Res.,* **104,** 25 833–25 851.

Snyder, R. L., F. W. Dobson, J. A. Elliott, and R. B. Long, 1981: Array measurements of atmospheric pressure fluctuations above surface gravity waves. *J. Fluid Mech.,* **102,** 1–59.

Stanton, T. E., D. Marshall, and R. Houghton, 1932: The growth of waves on water due to the action of the wind. *Proc. Roy. Soc.,* **137A,** 283–293.

Stewart, R. W., 1967: Mechanics of the air sea interface. *Phys. Fluids Suppl.,* **10,** 547–554.

Sykes, R. I., 1980: An asymptotic theory of incompressible turbulent flow over a small hump. *J. Fluid Mech.,* **101,** 647–670.

Thijsse, J. T., 1951: Growth of wind-generated waves and energy transfer. Gravity Waves, National Bureau of Standards, Washington Circular 521, 281–287.

Townsend, A. A., 1980: Sheared turbulence and additional distortion. *J. Fluid Mech.,* **55,** 719–735.

Ursell, F., 1956: Wave generation by wind. *Surveys in Mechanics,* G. K. Batchelor, Ed., Cambridge University Press, 216–249.

Uz, B. M., M. A. Donelan, T. Hara, and E. J. Bock, 2002: Laboratory studies of wind stress over surface waves. *Bound.-Layer Meteor.,* **102,** 301–331.

van Duin, C. A., and P. A. E. M. Janssen, 1992: An analytical model of the generation of surface gravity waves by turbulent air flow. *J. Fluid Mech.,* **236,** 197–215.

Walmsley, J. L., and P. A. Taylor, 1996: Boundary-layer flow over topography: Impacts of the Askervein study. *Bound.-Layer Meteor.,* **78,** 291–320.

Young, I. R., 1999: *Wind Generated Ocean Waves.* Elsevier, 288 pp.

——, and A. V. Babanin, 2001: Wind wave evolution in finite depth water. *Proc. 14th Australasian Fluid Mechanics Conf.,* Adelaide, Australia, Adelaide University, 79–86.

——, M. L. Banner, M. A. Donelan, A. V. Babanin, W. K. Melville, F. Veron, and C. McCormick, 2005: An integrated study of the wind wave source term balance in finite depth water. *J. Atmos. Oceanic Technol.,* **22,** 814–828.

Zeman, O., and N. O. Jenssen, 1987: Modification to turbulence characteristics in flow over hills. *Quart. J. Roy. Meteor. Soc.,* **113,** 55–80.